ACS OMEGA

Open Access

http://pubs.acs.org/journal/acsodf

Article

Fluid−Solid Coupling Characteristics of Methane-Containing Coal during Borehole Extraction of Coalbed: Numerical Modeling and Experimental Research

Li Yan, Hu Wen,* Yongfei Jin, Jun Guo, Yin Liu, and Shixing Fan

Cite This: *ACS Omega* 2023, 8, 49334−49346

Read Online

ACCESS | Metrics & More | Article Recommendations

ABSTRACT: The control and utilization of coalbed methane (CBM) are crucial for ensuring the safety of coal mining operations and mitigating greenhouse gas emissions. Predrainage of CBM from boreholes plays a pivotal role in preventing CBM accidents, harnessing CBM energy resources, and reducing greenhouse gas emissions. To better understand the evolution of key parameters during the predrainage process of CBM boreholes, this study, based on fundamental assumptions of coupling models, integrates the theories of elasticity, seepage mechanics, and fluid mechanics. It establishes a comprehensive mathematical model that reveals the interrelationships among the stress field, deformation field, and seepage field within methane-containing coal systems. By comparing numerical solutions with analytical solutions and conducting physical similarity simulation experiments, the study demonstrates the correctness of the methane-containing coal fluid−solid coupling model. The model developed in this study represents an improvement over traditional methane-containing coal seepage theories and fluid−solid coupling model theories and can be widely applied in the prevention of coal and CBM outbursts as well as CBM extraction.

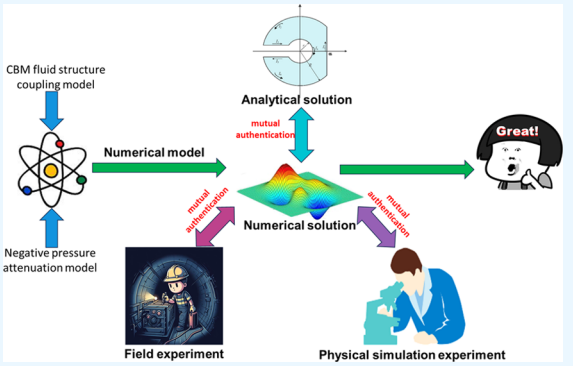

1. INTRODUCTION

Coalbed methane (CBM) is a high-heat, clean energy source, with a heat generation of about (3.35−3.77) × 10^5 J/m^3 of CBM,[1−3] equivalent to the heat of 1 kg of standard coal, and the pollution it produces is only 1/40 of that of oil and 1/800 of that of coal.[4−6] It can be seen that methane has a very large potential as a common fuel and chemical raw material.[7−9] For the mine types of CBM outburst mines and high CBM mines, the simultaneous extraction of coal and CBM is the best measure for the utilization of coal mine CBM resources and the control of CBM disasters.[10−12] The seepage law of CBM in coalbeds is one of the basic problems in the research field of coal mine CBM disaster prevention and control, which has important guiding significance for the basic theoretical research on CBM outburst, CBM extraction, and coal and CBM outburst prevention and control.[13−15]

Coal is a dual medium of pore fracture, and the deformation of coal and the flow of CBM during the mining process are under the fluid−solid coupling effect. Coal and gas outburst is also a disaster phenomenon caused by the instability and failure of coal under the fluid−solid coupling effect.[16,17] Therefore, if the migration law of the CBM in coalbeds is to be more in line with reality, the fluid−solid coupling problem of the CBM in coalbeds must be considered. Zou[18] studied the fluid−solid coupling characteristics of methane-containing coal in the hydraulic fracturing (HF) process and obtained the five-stage change characteristics of gas pressure response, strain change, and gas diffusion parameters and provided theoretical support and practical guidance for field test parameter selection to enhance the CBM recovery mechanism. Hu[19] applied the fundamental principles of fluid−solid coupling to investigate the correlation between porosity and permeability in coal. Their study delved into definitions related to coal's porosity and permeability and examined the impacts of adsorption expansion, changes in pore free gas pressure, and the Klinkenberg effect on gas flow in coal. However, they overlooked the influence of mobile water and residual water on the expansion stress in gas-bearing coal seams. Zhang[20] proposed a numerical simulation method of fluid−solid coupling, established the permeability model of elastic and plastic coal samples through the stress−permeability experimental results of elastic and plastic coal samples, and embedded it into FLAC3D software through uniaxial and triaxial flow simulation to verify the accuracy and

Received: October 8, 2023
Revised: November 11, 2023
Accepted: December 1, 2023
Published: December 12, 2023

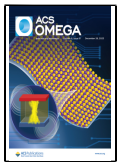

https://doi.org/10.1021/acsomega.3c07852
ACS Omega 2023, 8, 49334−49346

feasibility of the numerical simulation method. Zhou[21] proposed an improved thermal solid−fluid coupling model to simulate the process of coalbed injection flue gas (CO_2/N_2) to promote CBM extraction. The model successfully coupled the complex interactions, such as coal deformation, multicomponent gas and water multiflow, gas competitive adsorption, and heat transfer. Tao[22] conducted a study based on nine necessary THM coupling model basic assumptions; he comprehensively applied elastic mechanics, seepage mechanics, and heat transfer theory and established a realistic three-field two-way coupling mathematical model, revealing the interrelationship between seepage field, deformation field, and temperature field in methane-containing coal systems. Peng[23] used a self-developed triaxial servo-controlled permeation device and self-developed coal and CBM outburst simulation test device to study the influence mechanism of gas permeation on coal and CBM outburst disaster through experiments. Yin[24] used a self-made "coal-containing gas coal body thermal−fluid−solid three-way servo permutation coupling device" to conduct experimental research on anthropology from Zhaozhuang Mine Jincheng Coal Mine Group No. 3 Coalbed and explored the CBM term law of metal containing coal in the whole stress−strain process under constant gas pressure and condensing pressure conditions. Liu[25] established a fluid−solid coupling model based on an equivalent fracture coal model, with the aim of investigating the impact of hydraulic fracturing (HF) on coal seam stress unloading and permeability enhancement.

At present, domestic and foreign scholars have done a lot of research work on the related theory of CBM flow in coal,[26,27] but there is still an urgent need to improve the evolution law of porosity and permeability of methane-containing coal,[28] the fluid−solid coupling theory of methane-containing coal,[29] and especially in the simulation experiment of CBM borehole predrainage in this coalbed.[30] Furthermore, at the current stage, most of the research primarily concentrates on the coupled control equations between the gas phase and solid phase. However, it is essential to underscore that a significant amount of groundwater simultaneously exists within the coal seams. To gain a comprehensive understanding of the migration behavior and parameter variation patterns of coalbed methane during the pre-extraction process, it is imperative to comprehensively consider the influencing factors of the water phase within the deformation, permeability, and transport equations.

In order to address this research gap, this study aims to establish the control equations for the stress field of coalbed methane, taking into account the influence of the water phase. This involves a thorough investigation into the flow mechanisms of coalbed gas diffusion. The coal is considered a "dual-porosity medium", and equations governing porosity, fracture ratio, and permeability are incorporated, along with the diffusion equations for gas transport. These components collectively form a coupled flow-solid model for gas-bearing coal. Through an analysis of gas resistance in the pipelines, the attenuation patterns of negative pressure in pre-extraction gas drainage boreholes are derived. This study combines numerical solutions with analytical solutions and validates the model's reliability through a comparison of numerical results to field data and experimental outcomes. This effort lays a solid foundation for the subsequent exploration of the evolving patterns of key parameters in coalbed methane pre-extraction.

2. METHANE-CONTAINING COAL FLUID−SOLID COUPLING MODEL

2.1. Stress Field Governing Equation. Coal is a natural body with pores and fractures, where gas is mainly stored in the pores, and fractures are the flow channels for gas and water. Coal particles form a skeleton, and when a load is applied to the coal body, the skeleton deforms and fluid flows relative to the skeleton. Assuming that CBM flows in the coal body, ignoring the water flow, the inertial force of coal deformation, and the body force of fluid in the coal body, coal can be divided into small equilibrium units. Each unit maintains equilibrium. The equilibrium differential equation of the unit can be constructed according to Figure 1.

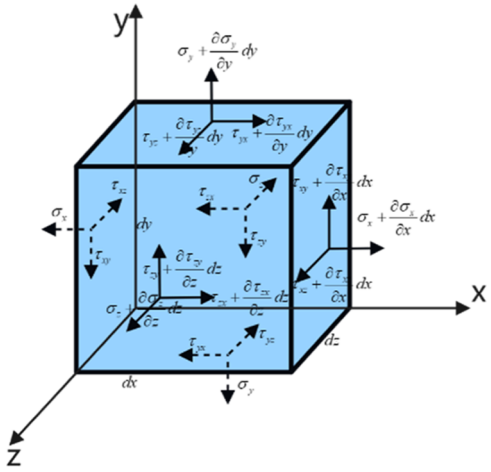

Figure 1. Schematic diagram of the stress state of a coal microhexahedron.

The stress components along the coordinate axes on the microelement are denoted by σ_x, σ_y, σ_z, τ_{xy}, τ_{xz}, τ_{yz}, τ_{yx}, τ_{zx}, and τ_{zy}, which are opposite to the directions of the coordinate axes. The directions of the stress components are consistent with the coordinate axes. According to the static equilibrium equation, the resultant force on the microelement in the x, y, and z directions is zero.

$$\begin{cases} \dfrac{\partial \sigma_x}{\partial x} + \dfrac{\partial \tau_{yx}}{\partial y} + \dfrac{\partial \tau_{zx}}{\partial z} + F_x = 0 \\ \dfrac{\partial \sigma_y}{\partial y} + \dfrac{\partial \tau_{xy}}{\partial x} + \dfrac{\partial \tau_{zy}}{\partial z} + F_y = 0 \\ \dfrac{\partial \sigma_z}{\partial z} + \dfrac{\partial \tau_{yz}}{\partial y} + \dfrac{\partial \tau_{xz}}{\partial z} + F_z = 0 \end{cases} \tag{1}$$

This can be written in tensor form as

$$\sigma_{ij} + F_i = 0 \quad (i, j = 1, 2, 3) \tag{2}$$

Combining the aforementioned expression with the effective stress equation proposed by Baptista-Pereira[31] based on experimental research, one can derive the following formula

$$\sigma_{ij,j}^{\text{eff}} + [\alpha(s_w p_w + s_g p_g)\delta_{ij}]_j + F_i = 0 \tag{3}$$

where $u(x, y, z)$, $v(x, y, z)$, and $w(x, y, z)$ are the displacement components in the x, y, and z directions, respectively, and the

https://doi.org/10.1021/acsomega.3c07852
ACS Omega 2023, 8, 49334−49346

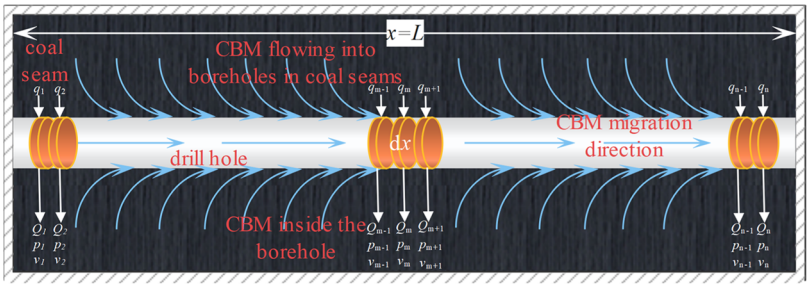

Figure 2. Schematic Diagram of CBM Flow within the Borehole

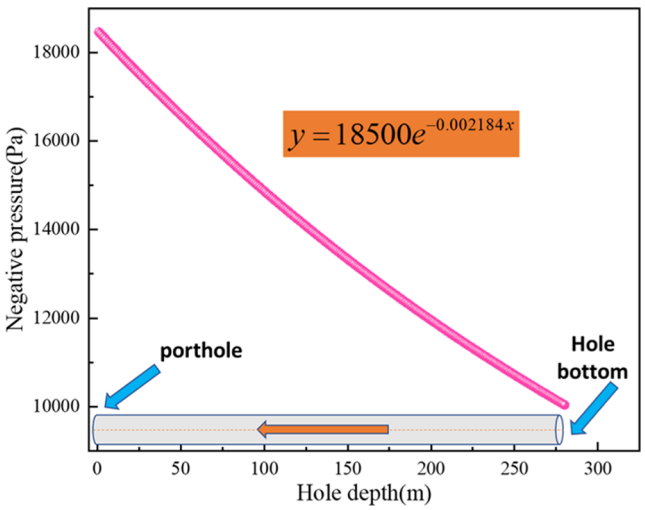

Figure 3. Graph depicting the negative pressure attenuation pattern along the borehole length.

relationship between strain components and displacement components can be expressed as follows[32]

$$\varepsilon_{ij} = \frac{1}{2}(u_{j,i} + u_{i,j}) \tag{4}$$

where F_i is the volumetric stress of the coal body, N/m^3; δ_{ij} is the Kronecker variable, taking the value of 1 when $i = j$, and 0 when $i \neq j$; ε_{ij} is strain component; $u_{i,j}(i, j = 1, 2, 3)$ is the displacement vector of a particle.

Based on the assumption that coal is an unsaturated porous medium, the strain of coal is composed of various factors, including geostress, moisture strain, strain caused by CBM pressure compressing coal, and strain caused by adsorption and desorption. In order to better describe the strain characteristics of coal, we can construct corresponding constitutive equations from these different aspects.[33] These equations can help us better understand the deformation law of coal and provide theoretical support for the development of CBM.

The strain caused by CBM pressure, the unidirectional linear moisture strain, the strain caused by effective stress, and the strain due to adsorption and desorption can be expressed as follows[34]

$$\varepsilon_p = -\frac{1}{K_m}(\overline{p} - \overline{p}_0) \tag{5}$$

$$\varepsilon_M = \beta_M(s_w - s_{w0}) \tag{6}$$

$$\varepsilon_\sigma = \frac{1}{2G}\left(\sigma_{\text{eff}} - \frac{\upsilon}{1+\upsilon}\sigma_\upsilon^{\text{eff}}\right) \tag{7}$$

$$\varepsilon_s = \alpha_{sg}V_{sg} = \alpha_{sg}\frac{V_L p}{p + p_L}\exp\left[-\frac{c_2}{1 + c_1 p}(T - T_t)\right] \tag{8}$$

where K_m is the bulk modulus of the coal matrix, β_M is the coefficient of moisture expansion; α_{sg} is the volumetric strain coefficient induced by adsorption and desorption, kg/m^3; V_{sg} is the adsorbed CBM content, m^3/kg; c_1 is the pressure coefficient, MPa^{-1}; c_2 is the temperature coefficient, K^{-1}; V_L is the Langevin volume constant, m^3·kg^{-1}; p_L is the Langevin pressure constant, Pa; T is the coalbed temperature, K; T_t is the reference temperature in adsorption−desorption experiments, K, value is 298.

Then, the total deformation in one direction within the coal matrix is as follows

$$\begin{aligned}\varepsilon &= \varepsilon_p + \varepsilon_M + \varepsilon_\sigma + \varepsilon_s \\ &= -\frac{1}{3K_m}\Delta\overline{p} + \frac{\beta_M}{3}(s_w - s_{w0}) + \frac{1}{2G}\left(\sigma_{\text{eff}} - \frac{\upsilon}{1+\upsilon}\sigma_\upsilon^{\text{eff}}\right) + \frac{1}{3}\varepsilon_s\end{aligned} \tag{9}$$

$$\sigma_{\text{eff}} = 2G\varepsilon + \frac{\upsilon}{1+\upsilon}\sigma_\upsilon^{\text{eff}} + 2G\left[\frac{1}{3K_m}\Delta\overline{p} - \frac{\beta_M}{3}(s_w - s_{w0}) - \frac{1}{3}\varepsilon_s\right] \tag{10}$$

In the field of rock mechanics,[35] the following equation is applicable

$$\sigma_\upsilon^{\text{eff}} = \frac{E}{1 - 2\upsilon}\varepsilon_\sigma \tag{11}$$

Introducing the Lamé constant into the above equation, we can rewrite eq 10 as follows

$$\sigma_{\text{eff}} = 2G\varepsilon + \lambda\theta + \theta_p\Delta\overline{p} - \theta_M(s_w - s_{w0}) - \theta_s\varepsilon_s \tag{12}$$

where E is the elastic modulus; υ is Poisson's ratio; λ and G are Lamé constants, $\lambda = \frac{2G}{1-2\upsilon}$; θ_p, θ_M, and θ_s represent the stress coefficients induced by pressure, moisture-induced strain coefficients, and adsorption−desorption stress coefficients, respectively.

Substituting the above equations into the constitutive equation and equilibrium equation, we can derive the following expression

https://doi.org/10.1021/acsomega.3c07852
ACS Omega 2023, 8, 49334−49346

$$Gu_{i,jj} + \frac{G}{1-2\upsilon}u_{j,ji} + \theta_p(\Delta\overline{p})_{,i} - \theta_M(s_w - s_{w0})_{,i} - \theta_s(\varepsilon_s)_{,i} - \alpha\overline{p}_{,i} + F_i = 0 \tag{13}$$

2.2. Governing Equations for CBM Matrix Porosity and Permeability. Taking into account the dynamic variations in porosity and permeability of coal under the influence of gas−solid coupling is a prerequisite for studying the deformation of disturbed coal bodies and the gas−solid coupling mechanisms that lead to the migration of CBM. The determination of porosity can be expressed using the following formula[36]

$$\phi_m = \frac{V_p}{V_m} = \frac{V_{p0} + \Delta V_p}{V_{m0} + \Delta V_m} = 1 - \frac{V_{s0} + \Delta V_s}{V_{m0} + \Delta V_m} = 1 - \frac{1-\phi_{m0}}{1+\varepsilon_m}\left(1 + \frac{\Delta V_s}{V_{s0}}\right) \tag{14}$$

where V_p is the porosity volume; V_m is the coal matrix volume; V_{p0} is the initial porosity volume; V_{m0} is the initial coal matrix volume; V_{s0} is the initial skeleton volume; ΔV_p represents changes in porosity volume; ΔV_m represents changes in coal matrix volume; ΔV_s represents changes in skeleton volume; φ_{m0} is the initial porosity ratio; ε_m is the coal matrix volume strain.

The intrinsic deformation of coal particles in unsaturated porous media is the sum of strains induced by CBM pressure, strains resulting from adsorption and desorption processes, and moisture-induced strains.

$$\frac{\Delta V_s}{V_{s0}} = \varepsilon_p + \varepsilon_M + \varepsilon_s = -\frac{(\overline{p} - \overline{p}_0)}{K_m} + \beta_M(s_w - s_{w0}) + \alpha_{sg}V_{sg} \tag{15}$$

It has been determined through a combination of experimentation and theoretical derivation that the deformation of the coal matrix can be approximated as follows[37]

$$\varepsilon_m = \exp(-K_Y\Delta\sigma^{\text{eff}}) - 1 \tag{16}$$

where K_Y is the volume compression coefficient, MPa^{-1}.

Substituting eqs 15 and 16 into eq 14 yields a dynamic model for matrix porosity in the gas−water two-phase flow stage under compression conditions

$$\phi_m = 1 - \frac{1-\phi_{m0}}{\exp(-K_Y\Delta\sigma^{\text{eff}})}\left[1 - \frac{(\overline{p} - \overline{p}_0)}{K_m} + \beta_M(s_w - s_{w0}) + \alpha_{sg}V_{sg}\right] \tag{17}$$

Liu and Seidle[38−40] demonstrate that there is the following relationship between porosity and permeability

$$\frac{k_m}{k_{m0}} = \left(\frac{\phi_m}{\phi_{m0}}\right)^3 \tag{18}$$

In that case, permeability can be expressed by the following equation

$$k_m = k_{m0}\left\{\frac{1}{\phi_{m0}} - \frac{1-\phi_{m0}}{\phi_{m0}\cdot\exp(-K_Y\Delta\sigma^{\text{eff}})}\left[1 - \frac{(\overline{p} - \overline{p}_0)}{K_m} + \beta_M(s_w - s_{w0}) + \alpha_{sg}V_{sg}\right]\right\}^3 \tag{19}$$

2.3. Governing Equations for the CBM Matrix Fracture and Permeability. Considering the width within the coal matrix as a and the width of the fractures as b, the fracture porosity within the coal matrix can be expressed as follows

$$\phi_f = \frac{(a+b)^3 - a^3}{(a+b)^3} \tag{20}$$

Due to the fact that in coalbeds, the width of fractures is significantly smaller than the width of the coal matrix, i.e., $b \ll a$, then

$$\phi_f \approx \frac{3b}{a} \tag{21}$$

The deformation of the coal matrix and fractures in any direction can be expressed as follows[41]

$$\mathrm{d}\varepsilon_v = \frac{b}{a}\mathrm{d}\varepsilon_f + \mathrm{d}\varepsilon_m \tag{22}$$

Taking the partial derivative on both sides with respect to fracture porosity, we obtain

$$\mathrm{d}\phi_f = \phi_f\left(\frac{a+b}{a}\mathrm{d}\varepsilon_f - \mathrm{d}\varepsilon_v\right) = \phi_f(\mathrm{d}\varepsilon_f - \mathrm{d}\varepsilon_v) \tag{23}$$

The intrinsic deformation of coal particles in unsaturated porous media is the sum of strains induced by effective stress, strains resulting from adsorption and desorption processes, and moisture-induced strains.

$$\mathrm{d}\varepsilon_v = \mathrm{d}\varepsilon_\sigma + \mathrm{d}\varepsilon_s + \mathrm{d}\varepsilon_M = -\frac{1}{K_m}\mathrm{d}\sigma_m^{\text{eff}} + \mathrm{d}\alpha_{sg}V_{sg} + \beta_M\mathrm{d}(s_w - s_{w0}) \tag{24}$$

$$\mathrm{d}\varepsilon_f = -\frac{1}{K_f}\mathrm{d}\sigma_f^{\text{eff}} \tag{25}$$

Substituting eqs 24 and 25 into eq 23, we have

$$\frac{\phi_f}{\phi_{f0}} = \exp\left[-\frac{1}{K_f}\Delta\sigma_f^{\text{eff}} + \frac{1}{K_m}\Delta\sigma_m^{\text{eff}} - \alpha_{sg}V_{sg} - \beta_M(s_w - s_{w0})\right] \tag{26}$$

where ε_f is the volume strain of fractures; ε_v is the intrinsic deformation of coal particles in unsaturated porous media; $\sigma_m^{eff} = \overline{\sigma} + \beta_m\overline{p}_m$, $\sigma_m^{eff} = \overline{\sigma} + \beta_f\overline{p}_f$; β_m, β_f are the Biot coefficients for both the matrix and fractures; $\overline{\sigma}$ is the average stress in coal body, $\overline{\sigma} = -(\sigma_{xx} + \sigma_{yy} + \sigma_{zz})/3$; $\overline{p}_m$ is the average CBM pressure in the matrix; $\overline{p}_f$ is the average CBM pressure in the fractures.

Substituting eq 26 with eq 18 yields

https://doi.org/10.1021/acsomega.3c07852
ACS Omega 2023, 8, 49334−49346

$$\frac{k_f}{k_{f0}} = \exp\left[-\frac{3}{K_f}\Delta\sigma_f^{\text{eff}} + \frac{3}{K_m}\Delta\sigma_m^{\text{eff}} - 3\alpha_{sg}V_{sg} - 3\beta_M(s_w - s_{w0})\right] \tag{27}$$

2.4. CBM Seepage and Diffusion Control Equations. The continuous flow of CBM within the coal matrix actually signifies the conservation of CBM mass within the control volume. Within the time interval dt, the difference in total CBM mass entering and leaving control volume μ is given by

$$\text{div}(\mu) = -\frac{\partial M}{\partial t} \tag{28}$$

Based on the assumption that CBM flows through fractures in accordance with Darcy's law within the coalbed, and gas diffusion in the matrix follows Fick's law, in conjunction with the ideal gas state equation and the mass conservation equation, we can derive

$$\frac{\partial C_m}{\partial t} = -\frac{M_g}{\tau RT}(p_m - p_{fg}) \tag{29}$$

$$V = -\frac{k_f}{\mu_g}\nabla p_f \tag{30}$$

$$C_m = V_{sg}\rho_s\frac{M_g}{RT}p_n + \phi_m\frac{M_g}{RT}p_m \tag{31}$$

where C_m is the diffusion mass concentration of CBM in the matrix, kg/m^3; τ is the time for desorption diffusion of CBM, s; M_g is the molar mass of CBM, kg/mol; R is the ideal gas constant, 8.314 J/(mol·K); μ_g is the CBM dynamic viscosity, Pa·s; ρ_s is the skeleton density, kg/m^3; p_n is the standard atmospheric pressure, 101 kPa; p_m is the CBM pressure in the matrix, Pa.

Based on the above analysis, the equilibrium equation can be transformed into the diffusion and seepage transport equations for coalbed gas within the coal body

$$\frac{\partial}{\partial t}\left\{\left[\frac{V_L p_m}{p_m + p_L}\exp\left[-\frac{c_2}{1 + c_1 p_m}(T - T_t)\right]\rho_s\frac{M_g}{RT}p_n + \left[1 - \frac{1 - \phi_{m0}}{\exp(-K_Y\Delta\sigma^{\text{eff}})}\times\left[1 - \frac{(\bar{p} - \bar{p}_0)}{K_m} + \beta_M(s_w - s_{w0}) + \alpha_{sg}\frac{V_L p_m}{p_m + p_L}\exp\left(-\frac{c_2}{1 + c_1 p_m}(T - T_t)\right)\right]\right]\frac{M_g}{RT}p_m\right\} = -\frac{M_g}{\tau RT}(p_m - p_{fg}) \tag{32}$$

$$\frac{\partial(p_f\varphi_f)}{\partial t} - \nabla\left(p_f\frac{k_f}{\mu_g}\nabla p_f\right) = \frac{M_g}{\tau RT}(p_m - p_{fg}) \tag{33}$$

2.5. Variation Pattern of Negative Pressure along the Length of the Borehole during Extraction. When coalbed gas flows inside a borehole, it experiences frictional forces, resulting in resistance along the borehole's length. As coalbed gas continuously flows from the borehole wall into the borehole in advance coalbed drilling, the flow within the borehole is considered as a variable mass flow. To analyze this, the advance borehole is divided into several small elemental sections, and the variable mass flow velocity within each elemental section is treated as the average flow velocity. This allows us to consider the coalbed gas flow within each elemental section as a constant mass flow. The schematic diagram of coal seam airflow in the borehole is shown in Figure 2.

In general, collapse or deformation inside a borehole exhibits significant uncertainty and randomness. In theoretical calculations, we neglect the local losses caused by borehole deformation. Therefore, the combined loss can be expressed as

$$\Delta p_m = \lambda'_m\frac{\mathrm{d}x}{\mathrm{d}}\frac{\rho_m\overline{v}_m^2}{2} + \rho_m\frac{(v_{m+1}^2 - v_m^2)}{2} \tag{34}$$

where v_m and v_{m+1} are the flow velocities of CBM in the m-th segment, $v_m = \frac{Q_m}{\pi r_0^2}$; v_{m+1} is the flow velocity of CBM in the (m+1)-th segment, m/s, $v_{m+1} = \frac{Q_m + q_m}{\pi r_0^2}$; $\overline{v}_m$ is the average flow velocity in the m-th segment, $\overline{v}_m = \frac{v_m + v_{m+1}}{2} = \frac{2Q_m + q_m}{2\pi r_0^2}$; λ'_m is the corrected local resistance coefficient, N·s^2/m^4.

Zhang[42] elucidates the test results of CBM extraction experiments under various borehole deformation instability conditions. It proposes a method for calculating the along-hole resistance coefficient of borehole walls, as follows

$$\lambda'_m = 64(1 + 0.04304Re^{0.6142}),\ (Re \le 2320) \tag{35}$$

$$\lambda'_m = [1.14 - 2\lg(\varepsilon/d + 21.25Re^{-0.9})]^{-2} \times (1 + 0.0163Re^{0.2278}),\ (Re \ge 4000) \tag{36}$$

It is necessary to calculate the Reynolds number of the CBM flow in the m-th infinitesimal segment according to the formula below to clarify the flow regime of this segment and determine its along-borehole resistance coefficient.[43]

$$Re_m = \frac{2\rho_m(2Q_{m-1} + q_m)}{\mu\pi d} \tag{37}$$

where ρ_m is the average density of CBM in the m-th segment, kg/m^3; Q_m is the original CBM content within the m-th borehole segment, m^3; q_m is the amount of CBM influx into the borehole wall within the m-th segment, m^3.

The negative pressure extraction in each segment is calculated as follows

$$\Delta p_m = \frac{\mathrm{d}p(x)}{\mathrm{d}x} = \frac{8\rho(q(x)^2 + 2Q(x)q(x))}{\pi^2 d^4} + \frac{2\lambda'_m\rho(2Q(x) + q(x))^2}{\pi^2 d^5} \tag{38}$$

Liu[44] conducted numerous similar simulation experiments and derived the relationship between the flow rate within the borehole and the borehole length, as described by the equations below

https://doi.org/10.1021/acsomega.3c07852
ACS Omega 2023, 8, 49334−49346

$$q = \frac{\lambda}{r}\frac{p_0^2 - p_1^2}{\ln(R/r)} \tag{39}$$

$$q(x) = a \cdot e^{bx} \tag{40}$$

Based on the principles of mass conservation and the flow rate conservation equation, by simultaneously combining eqs 34 to 40 and setting the boundary conditions as $x = 0$, $q(0) = q_1$, and $q(L) = q_L$, we can solve for the negative pressure attenuation pattern along the borehole length.

$$p(x) = \frac{8\rho q_1^2\left(1 + \frac{L^2 q_1}{Q - Lq_1}\right)e^{4x/L\left(\frac{Q}{Lq_1}-1\right)}}{\pi^2 d^4 \frac{4}{L}\left(\frac{Q}{Lq_1} - 1\right)} + \frac{2\lambda_m' \rho q_1^2\left(1 + \frac{L^2 q_1}{Q - Lq_1}\right)^2 e^{4x/L\left(\frac{Q}{Lq_1}-1\right)}}{\pi^2 d^5 \frac{4}{L}\left(\frac{Q}{Lq_1} - 1\right)} \tag{41}$$

For a known coalbed and borehole, if Q, q_1, L and λ_m' in eq 41 are known constants, then the above equation can be approximately considered as

$$p(x) = s_1 e^{-s_2 x} \tag{42}$$

where s_1 and s_2 are constant coefficients.

Utilizing the monitoring data from the 215 working face of Huangling No. 2 Coal Mine, it can be determined that the borehole's extraction pressure is −18.5 kPa, the flow rate at the borehole mouth is monitored at 0.1 m^3/min, the total length of the borehole is 280 m, the coalbed's permeability coefficient is 5.5 m^2/MPa^2·day, and the effective extraction radius of the borehole is 17.9 m (1 month after extraction commenced). By input of these data into the formula for the negative pressure attenuation along the borehole length, the distribution of borehole negative pressure can be obtained, as shown in Figure 3.

The results indicate that the negative pressure value is highest at the borehole mouth, corresponding to the lowest absolute pressure. As the distance from the borehole mouth increases, the negative pressure value gradually decreases and the absolute pressure gradually increases. In addition to airflow and pressure changes within the coalbed, frictional resistance along the borehole, including factors such as airflow resistance and borehole wall friction, is a significant contributor to negative pressure attenuation. With an increasing distance from the borehole mouth, the influence of airflow resistance and borehole wall friction becomes more pronounced, leading to a gradual decrease in negative pressure values and a corresponding increase in absolute pressure.

Moreover, the roughness of the borehole wall and the size of the borehole diameter also affect the pattern of negative pressure attenuation. By incorporation of all of the parameters, the values of α and β in eq 44 can be determined, allowing for the characterization of the negative pressure attenuation pattern within the borehole as depicted in the above figure.

$$y = 18500\, e^{-0.002184x} \tag{43}$$

3. MODEL VALIDATION

3.1. Verification of Analytical and Numerical Solution Models. Equation 44 is the radial flow model of CBM established by Sun,[45] which is widely used. This equation represents an approximate analytical solution for the radial flow field of CBM within coalbeds.

$$P(r, t) = P_1 + (P_0 - P_1)\mathrm{erf}\left[\frac{\ln(r/r_0)}{\sqrt{2\varphi_0 t}}\right], (0 < t < \infty, r_0 < r < \infty) \tag{44}$$

Taking Huangling No. 2 Coal Mine (in Yan'an, Shaanxi, China) as a reference site and assuming a constant CBM

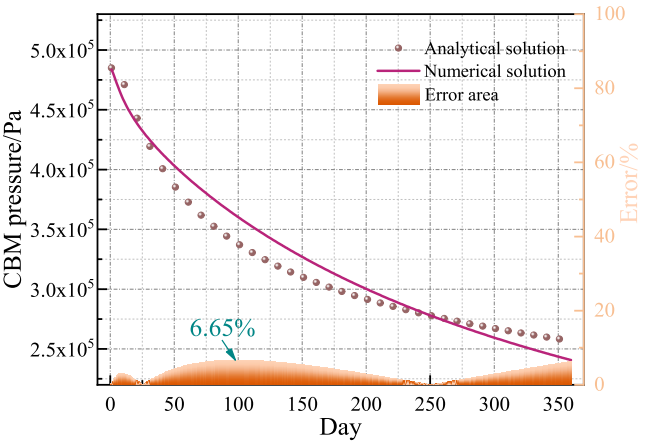

Figure 4. Comparison between numerical and analytical solutions.

Table 1. Borehole Information for Field Comparative Experiments

borehole number	borehole region (distance to the fourth Liaison lane) (m)	extraction negative pressure (kPa)	borehole diameter (mm)	borehole inclination (deg)	borehole length (m)
#316	3	−18.5	94	2	280
#338	132	−18.5	94	2	280
#344	168	−18.5	94	2	280
#389	438	−18.5	94	2	280
#379	378	−18.5	94	2	280

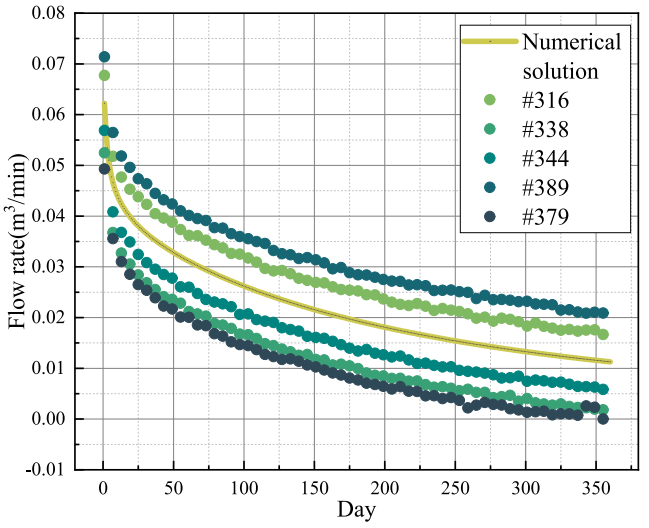

Figure 5. Comparison between numerical solutions and onsite extraction flow rates for each borehole.

https://doi.org/10.1021/acsomega.3c07852
ACS Omega 2023, 8, 49334−49346

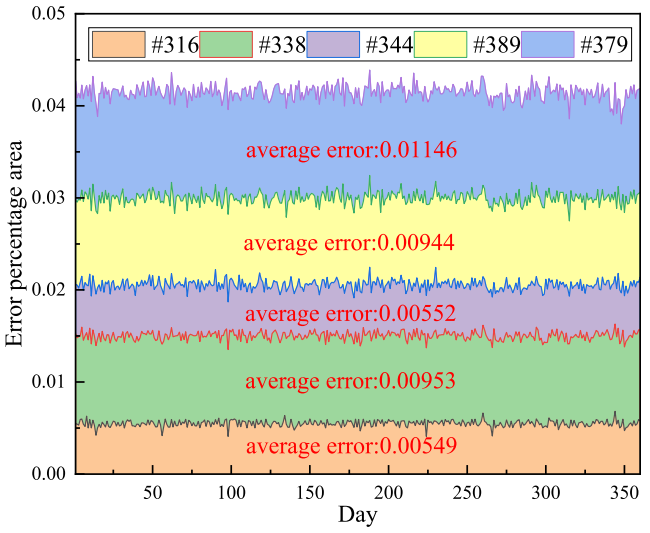

Figure 6. Area chart of percentage errors between numerical solutions and onsite extraction flow rates for each borehole.

pressure of 0.485 MPa, a negative extraction pressure of −18.5 kPa, an effective extraction radius of 17.9 m, and a borehole radius of 47 mm, numerical and analytical solutions for the temporal variation of the CBM pressure at a radial flow field radius of 1 m were calculated using the NUMPY package in PYTHON, as illustrated in Figure 4.

The results from the numerical solution of the gas-bearing coal fluid−solid coupling model in this study show relatively good agreement with the analytical solution, as indicated by the graph. Both solutions exhibit the same downward trend. During the initial phase of drainage, a pressure gradient is instantaneously formed between the coal seam and the interior of the borehole due to the impact of mining activities, leading to a sharp decrease in gas pressure at a distance of 1 m from the borehole. As mining progresses, the pressure gradient gradually declines and the gas pressure in the coal seam experiences a gentle decline. Both the numerical and analytical solutions adhered to this pattern.

However, due to the nonlinear second-order partial differential equation nature of the coupled model, the numerical solution is typically derived from specific numerical methods and discretization techniques, while the analytical solution is based on a series of assumptions and theoretical derivations. This can lead to an error between the analytical and numerical solutions, with a maximum value of 6.65% and a minimum value of 0, meaning that there are two intersections between the numerical and analytical solutions. By comparing the trends and characteristics of the numerical and analytical solutions, it can be seen that they largely adhere to the same pattern, suggesting that

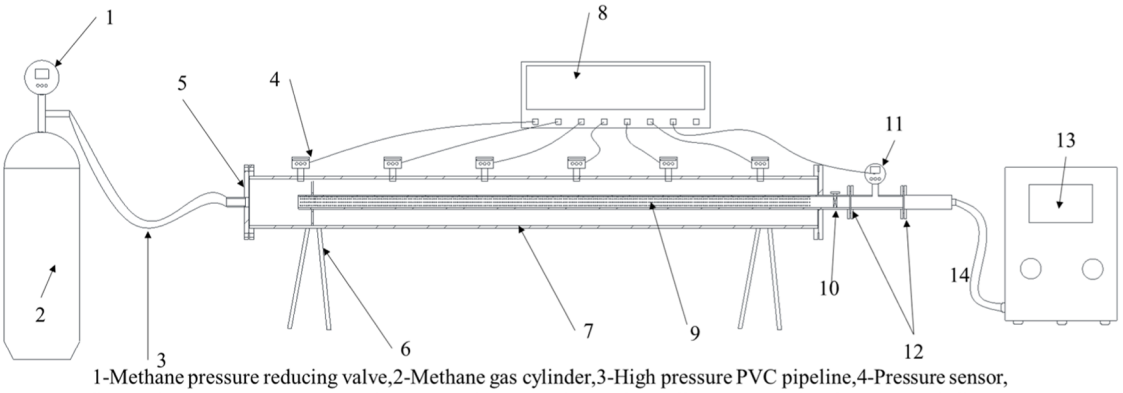

1-Methane pressure reducing valve,2-Methane gas cylinder,3-High pressure PVC pipeline,4-Pressure sensor, 5-flange plate,6-Pipe support,7-Coal seam simulation pipeline,8-data collector,9-Simulated extraction drilling, 10- Pipeline switch ,11-flow sensor,12-flange plate,13-negative pressure pump,14-Extraction connection PVC pipe

(a) Structural Diagram

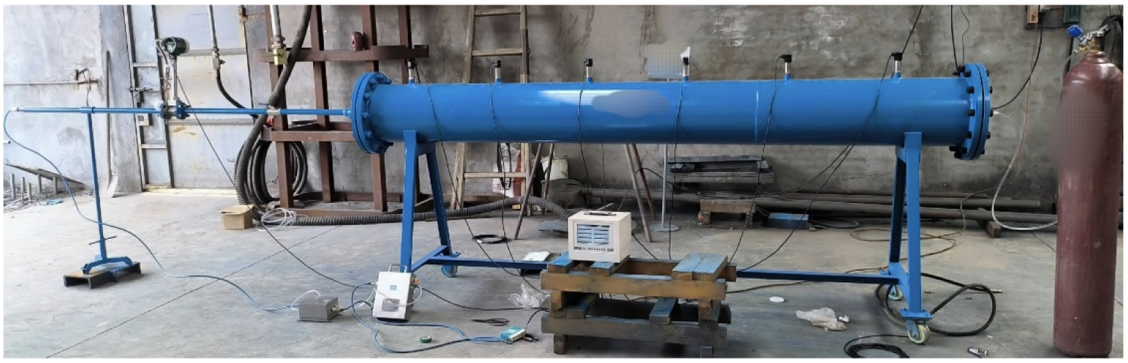

(b) Physical Image

Figure 7. Schematic diagram of the CBM pre-extraction borehole extraction simulation experimental system.

https://doi.org/10.1021/acsomega.3c07852
ACS Omega 2023, 8, 49334−49346

Table 2. Coal Particle Size Sieve Analysis Results[a]

particle size (mm)	+10	−10, +7	−7, +5	−5, +3	−3, +0.9	−0.9
mass (g)	40.25	84.44	90.15	91.21	94.31	99.64
frequentness (%)	8.05	16.888	18.03	18.242	18.862	19.928

[a]"+" indicates that the coal did not pass through that sieve, while "−" indicates that the coal passed through that sieve.

Table 3. Experimental Coal Sample Conditions

	average particle size d_{50} (mm)	weight of coal (kg)	volume of coal sample (m^3)	bulk density (g/cm^3)	void rate
coal sample	3.78	199.1776	0.20266345	0.9828	0.298

the gas-bearing coal fluid−solid coupling model is reasonably accurate.

3.2. Validation with Field Experimental Data. The comparison between the analytical and numerical solutions demonstrates the relative correctness and reliability of the methane-bearing coal−fluid coupling model established in this paper. To further illustrate the robustness of the coupling model, this section compares the numerical solutions with field monitoring data. The robustness of the methane-bearing coal−fluid coupling model presented in this section is verified by comparing the historical borehole CBM extraction flow rates from five boreholes monitored from the start of extraction to 180 days with the numerical simulation results. The borehole information is detailed in Table 1. The comparison between the calculated results and the experimental data is depicted in Figure 5.

With integration of the velocity in the entire cross section of the borehole according to Darcy's Law, the temporal variation of the borehole can be calculated. Based on the comparative data from monitoring of five boreholes in the target monitoring area, it can be observed that as CBM gradually depressurizes, the residual CBM pressure in the coalbed decreases and the methane concentration decreases as well. Therefore, during the CBM extraction process, the pure extraction flow rate of the CBM also gradually decreases with time. This phenomenon indicates that effective CBM extraction plays a positive role in reducing the methane concentration in the mine.

Furthermore, due to the different locations of the boreholes, the pure CBM flow rates within the boreholes also vary. This result suggests that the distribution of CBM in the coalbed is not uniform but rather exhibits some degree of variation. Therefore, when designing CBM extraction plans, it is essential to consider the rational arrangement of the borehole parameters to improve the effectiveness of CBM extraction.

Through field experiment data, we can observe that the CBM content is highest around borehole #389, while it is lowest around borehole #379. This discovery helps us more accurately identify high-risk areas of CBM in the coalbed, enabling the development of targeted extraction strategies.

Figure 6 shows the percentage error between the numerical solution of each borehole and the flow rate inside the borehole in the field experiment. Comparative analysis of the area chart of percentage errors between the flow rate data from the five boreholes and the numerical solutions reveals that while the onsite monitoring data exhibit oscillations due to environmental factors, fitting the errors results in a constant relationship. Additionally, because of the different distribution areas of the boreholes, there are varying ranges of errors, indicating differences in the CBM distribution within the coalbed. This further underscores the practicality of the research objectives in this study.

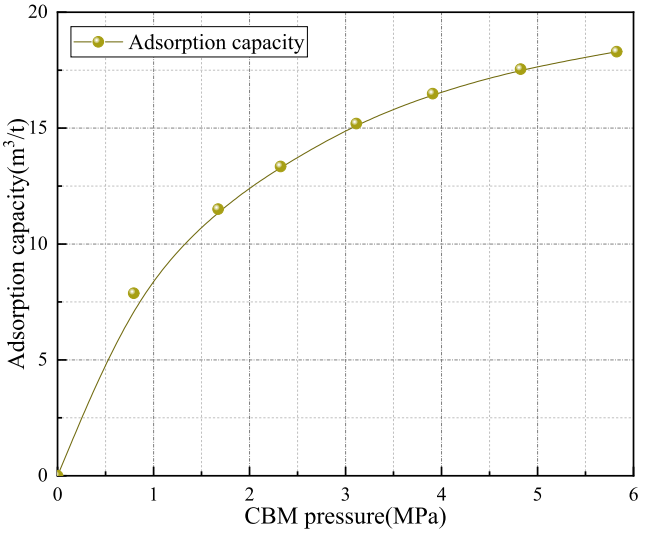

Figure 8. Isothermal adsorption curve of the coal sample.

It can be inferred that the trend of errors follows a pattern similar to that of the numerical solutions. This result indicates that the established coupling model is highly reliable and can effectively guide the practical implementation of CBM extraction despite the variability in monitoring data caused by environmental influences.

3.3. Physical Similarity Simulation Experiments. *3.3.1. Establishment of Experimental Platform.* Based on the methane-bearing coal−fluid coupling model established earlier, in order to investigate the spatiotemporal variations of key parameters during CBM extraction, verify the robustness of the coupling model, and better explore and validate the inversion model for in situ CBM pressure using monitoring data, a large-scale CBM pre-extraction borehole extraction simulation experimental system was independently developed. The schematic diagram of the system is shown in Figure 7. The system consists of five main components: a high-pressure gas source pressurization section, a CBM extraction borehole simulation section, a section for determining key CBM parameters, and a parameter data acquisition section.

The simulation pipeline consists mainly of two parts: the coalbed simulation pipeline and the simulation extraction borehole. The outer pipeline has an inner diameter of DN300,

Table 4. Proximate Analysis of Coal Samples

moisture content (M)	ash content (A)	volatile matter (V)	fixed carbon (Fc)	sulfur content (S)	heating value (Q)	adhesiveness index
2.62%	16.57%	33.71%	83.2%	0.52%	26.95 MJ/kg	26

https://doi.org/10.1021/acsomega.3c07852
ACS Omega 2023, 8, 49334−49346

Table 5. Parameter Values

parameter	values	parameter	values	parameter	values
E	1.18×10^9 Pa	K_m	9.26×10^9 Pa	υ	0.33
ρ_s	1.3×10^3 kg/m^3	K_s	1.5152×10^{10} Pa	ρ_w	1000 kg/m^3
μ_g	1.193×10^{-5} Pa·s	a	24 m^3/t	μ_w	1.01×10^{-3} Pa·s
α_{sg}	0.043 kg/m^3	b	5.88×10^{-7} Pa^{-1}	p_{f0}, p_{m0}	7×10^5 Pa
s_{w0}	0.4	c_1	0.07 MPa^{-1}	τ	153,360 s
P_L	2.45×10^6 Pa	K_Y	0.2 MPa^{-1}	V_L	0.016 m^3/kg
β_M	1×10^{-5} m^3/m^3	c_2	0.02 K^{-1}	φ_{m0}	0.298
k_{m0}	1.4×10^{-14} m^2	λ	5.5 m^2/MPa^2·day	φ_{f0}	0.3
k_{f0}	1.4×10^{-13} m^2	P_c	5×10^4 Pa	R	8.314 J/(mol·K)

a wall thickness of 5 mm, and a length of 3 m. To ensure gas tightness, both ends are sealed with flanges and metal gaskets. Additionally, pressure inlet and outlet holes are provided at both ends. To simulate the spatial variation of CBM parameters during borehole extraction, the outer pipeline has six threaded bases reserved at the top with diameters of 34 mm. Pressure sensors can be installed at these bases later. The distances of the threaded bases from the borehole mouth are 20, 70, 120, 170, 220, and 270 mm, respectively.

The inner pipeline has an inner diameter of DN65, a wall thickness of 2 mm, and a length of 2.8 m. To simulate the ventilation pathway inside the borehole, laser-cut flower holes with a diameter of 5 mm are evenly distributed in six directions on the inner pipe, with a linear distance of 6 mm between each pair of holes. Furthermore, to prevent coal dust from entering the depressurization pipeline through the flower holes during coal loading and depressurization, a 200 mesh sieve is wrapped around the outer surface of the inner pipe.

The design involves placing the inner pipe inside the outer pipe and filling the space between the pipe with experimental coal samples. This setup can replicate the conditions of CBM pre-extraction borehole extraction.

3.3.2. Coal Sample Preparation and Experimental Process. The coal sample used for simulating CBM pre-extraction borehole extraction is sourced from the 215 working face of Huangling No. 2 Coal Mine. The coal samples retrieved from the field were pulverized by using a jaw crusher. To closely replicate the onsite extraction environment, a mixture of particle sizes was employed. The desired particle sizes were obtained through sieving by using mesh screens. A 500g sample was selected to determine its particle size distribution and sample conditions, as detailed in Tables 2 and 3. In addition, industrial analysis was conducted on coal samples, and the results are shown in Table 4. The borehole inner pipe with mesh screens was inserted into the outer pipeline. The CBM pre-extraction borehole simulation pipeline, with one end designated for pressurization, was elevated by using a lifting vehicle. Prepared coal samples were sequentially loaded into the pipe by using a stepladder to simulate the CBM extraction process.

The simulation pipeline is connected to high-pressure methane gas cylinders, a vacuum pump, a negative pressure extraction pump, a flowmeter, sensors, and other equipment, ensuring airtight sealing in all parts.

Before pressurizing the experimental apparatus, in accordance with the requirements of "Preparation of Coal Samples" (GB474-2008), coal samples with a particle size of 0.17−0.25 mm and a mass of 35 g were prepared. Under constant temperature conditions of 30 °C and pressures ranging from 0.1−5.0 MPa, coal−gas isotherm adsorption experiments were conducted by using an HCA high-pressure gas adsorption apparatus. These experiments were carried out by using the volumetric method. Adsorption equilibria were established at different gas pressures, and the adsorbed gas amounts at various gas equilibrium pressures were determined. The adsorption isotherms are shown in Figure 8.

Based on the adsorbed gas quantities at different equilibrium gas pressures, the Langmuir equation[46] was regressed to calculate the gas adsorption constants for the experimental coal sample. The calculated values are as follows: the "a" value is 23.549 m^3/t, and the "b" value is 0.588 MPa^{-1}. The pressure relief valve was closed, the vacuum pump was opened to evacuate the coalbed, and then the methane gas cylinder was opened to inflate and adsorb in the coalbed. It was kept for 48 h to ensure that methane gas was adequately adsorbed in the coalbed. The gas injection hole was sealed, and parameters, such as pressure, temperature, and methane content, were monitored and recorded. Subsequently, the negative pressure extraction pump and the pressure relief valve were opened to release the gas to the external environment while recording data. Depressurization operations were stopped when the gas pressure in the test pipeline reached equilibrium with the external pressure.

4. RESULTS AND DISCUSSION

The comparison between the analytical and numerical solutions indicates that the calculation method for the established coal-fluid coupling model with methane is relatively accurate and reliable. Using the CBM pre-extraction borehole extraction simulation experimental platform established in the previous sections, a geometric model and boundary conditions consistent with the experimental setup were created. The conditions for the experimental platform setup were previously stated and are not reiterated here. In the geometric model, the bottom is considered a fixed boundary, the roof is subjected to a constant load boundary of 25 MPa, and the left and right sides are treated as sliding boundaries. In the initial conditions, the coalbed is in a state of free stress, with the pressure of the CBM in the matrix and fractures being equal everywhere. The established coal mass assembly model has no permeation and diffusion of the CBM at its four boundaries. The pressure boundary condition for the diffusion equation is the pressure of the CBM in the fractures, while the pressure boundary condition for the seepage equation is the extraction negative pressure.

The boundary conditions for the coal mass deformation field include displacement boundary conditions and stress boundary conditions

$$u_i = \gamma_i(x, y, z, t) \tag{45}$$

$$\sigma_{ij}\overline{n} = \psi_i(x, y, z) \tag{46}$$

https://doi.org/10.1021/acsomega.3c07852
ACS Omega 2023, 8, 49334−49346

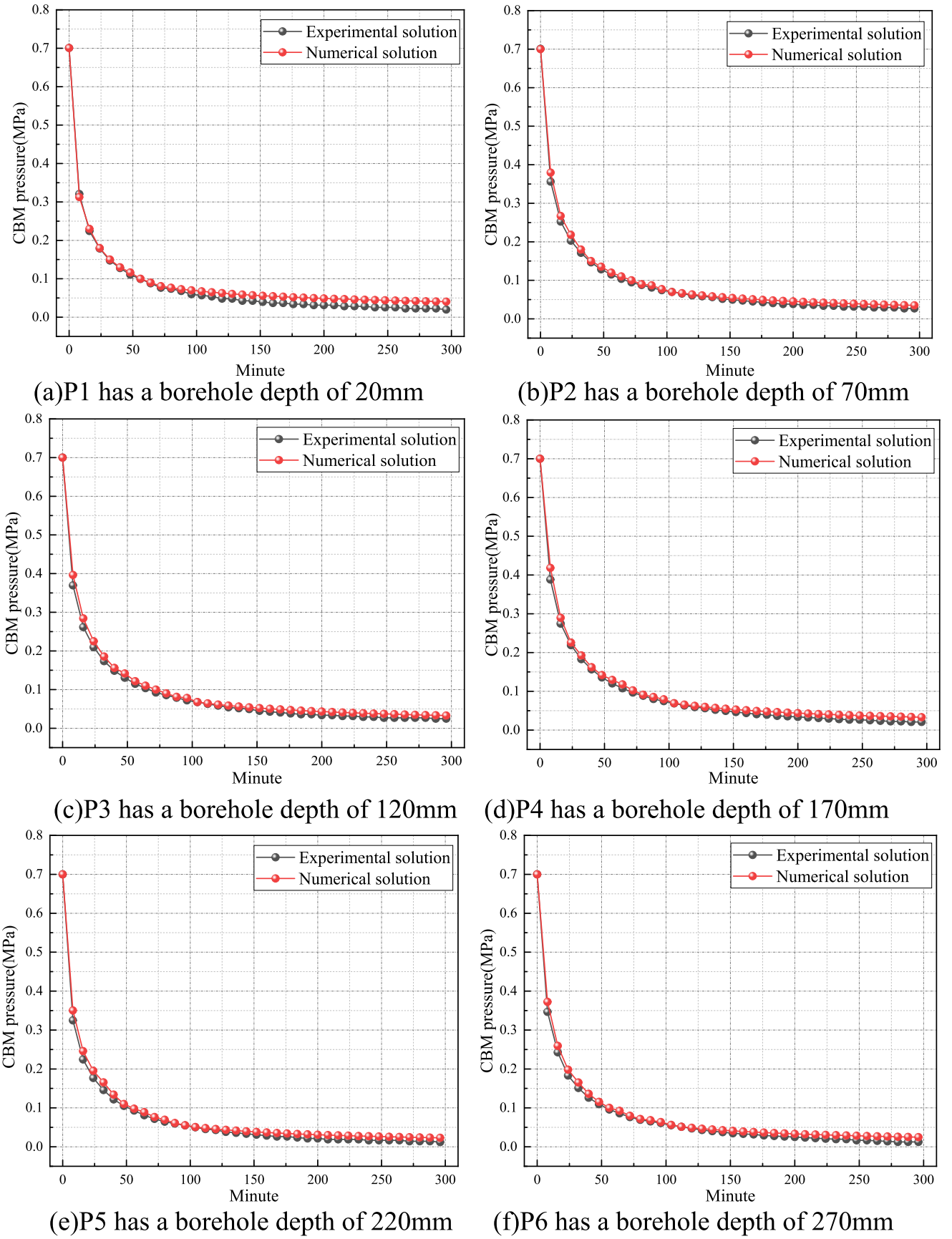

Figure 9. Comparison of measured and numerical simulation values of CBM pressure at different distances.

https://doi.org/10.1021/acsomega.3c07852
ACS Omega 2023, 8, 49334−49346

The flow boundary conditions for the CBM seepage field and diffusion field are as follows

$$\frac{k_f}{\mu}\nabla p_f \cdot \overline{n} = Q_f(x, y, z, t) \tag{47}$$

$$\frac{k_m}{\mu}\nabla p_m \cdot \overline{n} = Q_m(x, y, z, t) \tag{48}$$

where γ_i is the matrix displacement distribution function; ψ_i is the surface force distribution function; $\overline{n}$ is the directional derivative at boundary $\partial\Omega$; Q_m, Q_f is the given gas flow velocity at boundary $\partial\Omega$.

The values of each parameter in the numerical calculation are shown in Table 5.

The results of the measured and numerical simulation values of coalbed methane pressure at different distances in the experiment are plotted, as shown in Figure 9. From the experimental results and numerical simulation data, it can be observed that as time progresses, the gas pressure at various measurement points shows a significant decrease. The initial drop is more pronounced, which is due to the large pressure gradient between the gas pressure in the experimental coal body and the absolute pressure in the borehole during the initial extraction. This causes the desorbed gas to rapidly migrate from the high-pressure zone in the experimental coal body to the negative pressure zone inside the borehole. As gas gradually migrates, the gas pressure in the high-pressure zone decreases, and the pressure gradient decreases. During the extraction process, the gas pressure in the experimental coal body continues to decrease, and the curve of CBM pressure also becomes smoother until it reaches an equilibrium state.

At this point, the gas pressure in the experimental coal body and the pressure gradient between it and the absolute pressure in the borehole stabilize. The speed of desorbed gas migration gradually slows, ultimately reaching a dynamic equilibrium state. In the graph, the black data represent experimental results, and the red data represent numerical simulation results. Due to some assumptions made in numerical modeling, such as the assumption of coalbed isotropy and homogeneity, there are some discrepancies between experimental and numerical simulation data, leading to slight differences between the two sets of data.

However, from the data in the graph, it can be seen that both sets of data exhibit similar trends. In the initial stages, the CBM pressure decreases significantly, and as the pressure gradient decreases, the curve of the CBM pressure becomes smoother. The differences between individual data points are not substantial. Therefore, it can be concluded that the fluid−solid coupling model proposed in this paper meets the experimental requirements.

5. CONCLUSIONS

(1) A mathematical model of fluid−structure coupling in methane-containing coalbeds was developed based on fluid dynamics, elasticity theory, and seepage mechanics. This model includes stress field control equations, equations governing porosity, fractures, and permeability, as well as equations governing seepage and diffusion processes. It integrates the complex interactions in the coal−methane system during the process of predrainage drilling in coalbeds.

(2) The variation pattern of negative pressure during predrainage drilling in coalbeds was derived through the analysis of pipeline resistance. For a known coalbed and drilling hole, the negative pressure along the hole length follows the expression: $p(x) = s_1 e^{-s_2 x}$.

(3) By comparing the results of numerical solutions with analytical solutions, as well as comparing numerical solutions with field data, and considering the application of the model in the physical simulation experiments of coalbed gas drilling, the reliability and robustness of the methane-containing coal flow-solid coupling model have been demonstrated. This provides a solid foundation for the exploration of the evolution patterns of key parameters in the coalbed gas extraction process in subsequent mining operations.

(4) By utilizing this model in conjunction with monitoring data from drilling and extraction operations, it is possible to infer the in situ parameters of coalbed gas and residual gas content within the coal seam. This enables a more detailed exploration of coalbed gas parameters and facilitates the development of precise extraction control strategies.

AUTHOR INFORMATION

Corresponding Author

Hu Wen − *School of Safety Science and Engineering, Xi'an University of Science and Technology, Xi'an 710054, China; Key Laboratory of Mine and Disaster Prevention and Control of Ministry of Education, Xi'an University of Science and Technology, Xi'an, Shaanxi 710054, China*; Email: wenh@xust.edu.cn

Authors

Li Yan − *School of Safety Science and Engineering, Xi'an University of Science and Technology, Xi'an 710054, China; Key Laboratory of Mine and Disaster Prevention and Control of Ministry of Education, Xi'an University of Science and Technology, Xi'an, Shaanxi 710054, China*; orcid.org/0000-0002-6306-0436

Yongfei Jin − *School of Safety Science and Engineering, Xi'an University of Science and Technology, Xi'an 710054, China; Key Laboratory of Mine and Disaster Prevention and Control of Ministry of Education, Xi'an University of Science and Technology, Xi'an, Shaanxi 710054, China*

Jun Guo − *School of Safety Science and Engineering, Xi'an University of Science and Technology, Xi'an 710054, China; Key Laboratory of Mine and Disaster Prevention and Control of Ministry of Education, Xi'an University of Science and Technology, Xi'an, Shaanxi 710054, China*

Yin Liu − *School of Safety Science and Engineering, Xi'an University of Science and Technology, Xi'an 710054, China; Key Laboratory of Mine and Disaster Prevention and Control of Ministry of Education, Xi'an University of Science and Technology, Xi'an, Shaanxi 710054, China*

Shixing Fan − *School of Safety Science and Engineering, Xi'an University of Science and Technology, Xi'an 710054, China*

Complete contact information is available at: https://pubs.acs.org/10.1021/acsomega.3c07852

Notes

The authors declare no competing financial interest.

https://doi.org/10.1021/acsomega.3c07852
ACS Omega 2023, 8, 49334−49346

■ ACKNOWLEDGMENTS

This work was supported by the State Scholarship Fund of China Scholarship Council (202308610333) and the National Natural Science Foundation of China (52274227). The authors appreciate the editor and anonymous reviewers for their comments and suggestions on improving our research.

■ NOMENCLATURE

σ_x	positive stress component along the x-axis
σ_y	positive stress component along the y-axis
σ_z	positive stress component along the z-axis
τ_{xy}	shear stress component in the direction from the x-axis to the y-axis
τ_{xz}	shear stress component in the direction from the x-axis to the z-axis
τ_{yz}	shear stress component in the direction from the y-axis to the z-axis
τ_{yx}	shear stress component in the direction from the y-axis to the x-axis
τ_{zx}	shear stress component in the direction from the z-axis to the x-axis
τ_{zy}	shear stress component in the direction from the z-axis to the y-axis
$u(x, y, z)$	displacement component along the x-axis
$v(x, y, z)$	displacement component along the y-axis
$w(x, y, z)$	displacement component along the z-axis
F_i	the volumetric stress of coal body, N/m^3
δ_{ij}	Kronecker variable, taking the value of 1 when $i = j$, and 0 when $i \neq j$
ε_{ij}	strain components
$u_{i,j}(i, j = 1, 2, 3)$	displacement vector of a particle
K_m	bulk modulus of coal matrix
β_M	coefficient of moisture expansion
α_{sg}	volumetric strain coefficient induced by adsorption and desorption, kg/m^3
V_{sg}	adsorbed CBM content, m^3/kg
c_1	pressure coefficient, MPa^{-1}
c_2	temperature coefficient, K^{-1}
V_L	Langevin volume constant, m^3/kg
p_L	Langevin pressure constant, Pa
T	coalbed temperature, K
T_t	reference temperature in adsorption−desorption experiments, K, value is 298
E	elastic modulus
υ	Poisson ratio
λ, G	Lamé constant, $\lambda = \frac{2G}{1-2\upsilon}$
θ_p	stress coefficients induced by pressure
θ_M	moisture-induced strain coefficients
θ_s	adsorption−desorption stress coefficients
V_p	porosity volume
V_m	coal matrix volume
V_{p0}	initial porosity volume
V_{m0}	initial coal matrix volume
V_{s0}	initial skeleton volume
ΔV_p	changes in porosity volume
ΔV_m	changes in coal matrix volume
ΔV_s	changes in skeleton volume
φ_{m0}	initial porosity ratio
ε_m	coal matrix volume strain
K_Y	volume compression coefficient, MPa^{-1}
ε_f	volume strain of fractures
ε_v	intrinsic deformation of coal particles in unsaturated porous media
β_m, β_f	the Biot coefficients for both the matrix and fractures
$\overline{\sigma}$	average stress in coal body
$\overline{p}_m$	average CBM pressure in the matrix
$\overline{p}_f$	average CBM pressure in the fractures
C_m	diffusion mass concentration of CBM in the matrix, kg/m^3
τ	time for desorption diffusion of CBM, s
M_g	molar mass of CBM, kg/mol
R	ideal gas constant, 8.314 J/(mol·K)
μ_g	CBM dynamic viscosity, Pa·s
ρ_s	skeleton density, kg/m^3
p_n	standard atmospheric pressure, 101 kPa
p_m	CBM pressure in the matrix, Pa.
v_m, v_{m+1}	flow velocity of CBM in the m-th segment, m/s
$\overline{v}_m$	average flow velocity in the m-th segment, m/s
λ'_m	corrected local resistance coefficient, N·s^2/m^4
ρ_m	average density of CBM in the m-th segment, kg/m^3
Q_m	original CBM content within the m-th borehole segment, m^3
q_m	amount of CBM influx into the borehole wall within the m-th segment, m^3
s_1, s_2	constant coefficient

■ REFERENCES

(1) Nie, B.; Sun, S. Thermal recovery of offshore coalbed methane reservoirs: Flow characteristics of superheated steam in wellbores. *Energy* **2023**, *266*, No. 126245.
(2) Zhang, F.; Wang, S.; Duan, Y.; Chen, W.; Li, Z.; Li, Y. Thermodynamic assessment of hydrothermal combustion assisted fossil fuel in-situ gasification in the context of sustainable development. *Fuel* **2023**, *335*, No. 127053.
(3) Tao, S.; Chen, S.; Pan, Z. Current status, challenges, and policy suggestions for coalbed methane industry development in China: A review. *Energy Sci. Eng.* **2019**, *7* (4), 1059−1074.
(4) Soleimani, F.; Si, G.; Roshan, H.; Zhang, Z. Numerical modelling of coal and gas outburst initiation using energy balance principles. *Fuel* **2023**, *334*, No. 126687.
(5) Jakšić, O.; Jakšić, Z.; Guha, K.; Silva, A. G.; Laskar, N. M. Comparing artificial neural network algorithms for prediction of higher heating value for different types of biomass. *Soft Comput.* **2023**, *27* (9), 5933−5950.
(6) Yan, L.; Wen, H.; Liu, W.; Jin, Y.; Liu, Y.; Li, C. Adiabatic spontaneous coal combustion period derived from the thermal effect of spontaneous combustion. *Energy* **2022**, *239*, No. 122101.
(7) Wen, H.; Yan, L.; Jin, Y.; Wang, Z.; Guo, J.; Deng, J. Coalbed methane concentration prediction and early-warning in fully mechanized mining face based on deep learning. *Energy* **2023**, *264*, No. 126208.
(8) Finke, C. E.; Leandri, H. F.; Karumb, E. T.; Zheng, D.; Hoffmann, M. R.; Fromer, N. A. Economically advantageous pathways for reducing greenhouse gas emissions from industrial hydrogen under common, current economic conditions. *Energy Environ. Sci.* **2021**, *14* (3), 1517−1529.
(9) Lau, H. C.; Li, H.; Huang, S. Challenges and opportunities of coalbed methane development in China. *Energy Fuels* **2017**, *31* (5), 4588−4602.
(10) Lu, Y. Y.; Zhang, H. D.; Zhou, Z.; Ge, Z. L.; Chen, C. J.; Hou, Y. D.; Ye, M. L. Current status and effective suggestions for efficient exploitation of coalbed methane in China: a review. *Energy Fuels* **2021**, *35* (11), 9102−9123.

https://doi.org/10.1021/acsomega.3c07852
ACS Omega 2023, 8, 49334−49346

(11) Zhang, C.; Bai, Q.; Chen, Y.Using Stress Path-Dependent Permeability Law to Evaluate Permeability Enhancement and Coalbed Methane Flow in Protected Coal Seam: A Case Study. In *Geomechanics and Geophysics for Geo-Energy and Geo-Resources*; Springer, 2020; Vol. *6*, pp 1−25.
(12) Qin, Y.; Moore, T. A.; Shen, J.; Yang, Z.; Shen, Y.; Wang, G. Resources and geology of coalbed methane in China: a review. *Int. Geol. Rev.* **2018**, *60* (5−6), 777−812.
(13) Li, L.; Liu, D.; Cai, Y.; Wang, Y.; Jia, Q. Coal structure and its implications for coalbed methane exploitation: a review. *Energy Fuels* **2021**, *35* (1), 86−110.
(14) Fu, J.; Li, X.; Wang, Z. A novel sealing material and a bag-grouting sealing method for underground CBM drainage in China. *Constr. Build. Mater.* **2021**, *299*, No. 124016.
(15) Yang, X.; Wen, G.; Lu, T.; Wang, B.; Li, X.; Cao, J.; Lv, G.; Yuan, G. Optimization and field application of CO 2 gas fracturing technique for enhancing CBM extraction. *Nat. Resour. Res.* **2020**, *29*, 1875−1896.
(16) Zhang, J.; Li, B.; Liu, Y.; Li, P.; Fu, J.; Chen, L.; Ding, P. Dynamic multifield coupling model of gas drainage and a new remedy method for borehole leakage. *Acta Geotech.* **2022**, *17* (10), 4699−4715.
(17) Lin, H.; Ji, P.; Kong, X.; Li, S.; Long, H.; Xiao, T.; Li, B. Experimental study on the influence of gas pressure on CH4 adsorption-desorption-seepage and deformation characteristics of coal in the whole process under triaxial stress. *Fuel* **2023**, *333*, No. 126513.
(18) Zou, Q.; Lin, B. Fluid−solid coupling characteristics of gas-bearing coal subjected to hydraulic slotting: An experimental investigation. *Energy Fuels* **2018**, *32* (2), 1047−1060.
(19) Hu, S.; Liu, X.; Li, X. Fluid−solid coupling model and simulation of gas-bearing coal for energy security and sustainability. *Processes* **2020**, *8* (2), 254.
(20) Zhang, C.; Liu, J.; Zhao, Y.; Zhang, L.; Guo, J. A fluid-solid coupling method for the simulation of gas transport in porous coal and rock media. *Energy Sci. Eng.* **2019**, *7* (5), 1913−1924.
(21) Zhou, L.; Zhou, X.; Fan, C.; Bai, G.; Yang, L.; Wang, Y. Modelling of flue gas injection promoted coal seam gas extraction incorporating heat-fluid-solid interactions. *Energy* **2023**, *268*, No. 126664.
(22) Tao, Y.; Xu, J.; Liu, D.; Liang, Y. Development and validation of THM coupling model of methane-containing coal. *Int. J. Min. Sci. Technol.* **2012**, *22* (6), 879−883.
(23) Peng, S. J.; Xu, J.; Yang, H. W.; Liu, D. Experimental study on the influence mechanism of gas seepage on coal and gas outburst disaster. *Saf. Sci.* **2012**, *50* (4), 816−821.
(24) YIN, G. Z.; JIANG, C. B.; HU, J.; PENG, S. J.; LI, W. P. Experimental study of thermo-fluid-solid coupling seepage of coal containing gas. *J. China Coal Soc.* **2011**, *36* (9), 1495−1500.
(25) Liu, T.; Lin, B.; Fu, X.; Zhao, Y.; Gao, Y.; Yang, W. Modeling coupled gas flow and geomechanics process in stimulated coal seam by hydraulic flushing. *Int. J. Rock Mech. Min. Sci.* **2021**, *142*, No. 104769.
(26) Yang, Y.; Liu, S. Integrated modeling of multi-scale transport in coal and its application for coalbed methane recovery. *Fuel* **2021**, *300*, No. 120971.
(27) Liang, W.; Yan, J.; Zhang, B.; Hou, D. Review on coal bed methane recovery theory and technology: recent progress and perspectives. *Energy Fuels* **2021**, *35* (6), 4633−4643.
(28) Wei, M.; Wang, E.; Liu, X. Assessment of gas emission hazard associated with rockburst in coal containing methane. *Process Saf. Environ. Prot.* **2020**, *135*, 257−264.
(29) Xu, Y.; Liu, T.; Lin, B. Multi-field coupling theory and research progress of methane extraction in deep coal seams: A review. *J. Nat. Gas Sci. Eng.* **2022**, *107*, No. 104796.
(30) Wen, H.; Cheng, X.; Chen, J.; Zhang, C.; Yu, Z.; Li, Z.; Cheng, B.; et al. Micro-pilot test for optimized pre-extraction boreholes and enhanced coalbed methane recovery by injection of liquid carbon dioxide in the Sangshuping coal mine. *Process Saf. Environ. Prot.* **2020**, *136*, 39−48.
(31) Baptista-Pereira, C.; da Silva, B. G.; Meegoda, J. N. A Review of Theories to Calculate Pore Pressures when Fluids Penetrate into Rocks. *Mech. Res. Commun.* **2023**, *132*, No. 104184.
(32) Kong, X.; He, D.; Liu, X.; Wang, E.; Li, S.; Liu, T.; Yang, S.; et al. Strain characteristics and energy dissipation laws of gas-bearing coal during impact fracture process. *Energy* **2022**, *242*, No. 123028.
(33) Lou, Y.; Wu, Z.; Sun, W.; Yin, S.; Wang, A.; Liu, H.; Zuo, Y. Study on failure models and fractal characteristics of shale under seepage-stress coupling. *Energy Sci. Eng.* **2020**, *8* (5), 1634−1649.
(34) Xu, H.; Lai, X.; Shan, P.; Yang, Y.; Zhang, S.; Yan, B.; Zhang, N.; Zhang, N. Energy dissimilation characteristics and shock mechanism of coal-rock mass induced in steeply-inclined mining: Comparison based on physical simulation and numerical calculation. *Acta Geotechnica* **2023**, *18* (2), 843−864.
(35) Hao, D.; Tu, S.; Zhang, C.; Tu, H. Quantitative characterization and three-dimensional reconstruction of bituminous coal fracture development under rock mechanics testing. *Fuel* **2020**, *267*, No. 117280.
(36) Fan, Z.; Fan, G.; Zhang, D.; Zhang, L.; Zhang, S.; Liang, S.; Yu, W. Optimal injection timing and gas mixture proportion for enhancing coalbed methane recovery. *Energy* **2021**, *222*, No. 119880.
(37) Tao, Y.; Liu, D.; Xu, J.; Peng, S.; Nie, W. Investigation of the Klinkenberg effect on gas flow in coal matrices: A numerical study. *J. Nat. Gas Sci. Eng.* **2016**, *30*, 237−247.
(38) Liu, J.; Elsworth, D. Evaluation of pore water pressure fluctuation around an advancing longwall face. *Adv. Water Resour.* **1999**, *22* (6), 633−644.
(39) Liu, J.; Chen, Z.; Elsworth, D.; Qu, H.; Chen, D. Interactions of multiple processes during CBM extraction: a critical review. *Int. J. Coal Geol.* **2011**, *87* (3−4), 175−189.
(40) Seidle, J. P.; Jeansonne, M. W.; Erickson, D. J. In *Application of Matchstick Geometry to Stress Dependent Permeability in Coals*, SPE Rocky Mountain Petroleum Technology Conference/Low-Permeability Reservoirs Symposium SPE-24361, 1992.
(41) Xu, J.; Tang, X.; Li, S.; Tao, Y.; Jiang, Y. Space-time evolution rules study on acoustic emission location in rock under cyclic loading. *Front. Archit. Civ. Eng. China* **2009**, *3*, 422−427.
(42) Zhang, X.; Wang, W.; Shen, S. Experimental study on negative pressure and flow distribution during coalbed methane extraction under borehole deformation instability conditions. *Coal Sci. Technol.* **2020**, *48* (10), 45−51.
(43) Liu, J.; Wu, Z.; Lu, P.; Liu, Z.; Su, M. Study on effective extraction radius of directional long borehole and analysis of the influence mechanism. *ACS Omega* **2023**, *8* (2), 2344−2356.
(44) Liu, J.; Zhang, L. W.; Wang, L.; Chen, X. J. Negative pressure distribution of variable mass flow in coal mine drainage boreholes. *Energy Sources, Part A* **2020**, 1−18.
(45) Sun, P. Basic Models of Coalbed Methane Dynamics. *Xi'an Min. Inst. J.* **1989**, *2*, 7−13.
(46) Lin, H.; Ji, P.; Kong, X.; Li, S.; Long, H.; Xiao, T.; Li, B. Experimental study on the influence of gas pressure on CH4 adsorption-desorption-seepage and deformation characteristics of coal in the whole process under triaxial stress. *Fuel* **2023**, *333*, No. 126513.

https://doi.org/10.1021/acsomega.3c07852
ACS Omega 2023, 8, 49334−49346